High-Performance Microsupercapacitors Based on Two-Dimensional Graphene/Manganese Dioxide/Silver Nanowire Ternary Hybrid Film

Wenwen Liu,[†,¶] Congxiang Lu,[†,‡,¶] Xingli Wang,[†] Roland Yingjie Tay,[†] and Beng Kang Tay[*,†,‡]

[†]Novitas, Nanoelectronics Center of Excellence, School of Electrical and Electronic Engineering, Nanyang Technological University, Singapore 639798, Singapore and [‡]CINTRA CNRS/NTU/THALES, Nanyang Technological University, Singapore 637553, Singapore. [¶]These two authors contributed equally to this work.

ABSTRACT Microsupercapacitors (MSCs), as one type of significant power source or energy storage unit in microelectronic devices, have attracted more and more attention. However, how to reasonably design electrode structures and exploit the active materials to endow the MSCs with excellent performances in a limited surface area still remains a challenge. Here, a reduced graphene oxide (RGO)/manganese dioxide (MnO_2)/silver nanowire (AgNW) ternary hybrid film (RGMA ternary hybrid film) is successfully fabricated by a facile vacuum filtration and subsequent thermal reduction, and is used directly as a binder-free electrode for MSCs. Additionally, a flexible, transparent, all-solid state RMGA-MSC is also built, and its electrochemical performance in an ionic liquid gel electrolyte are investigated in depth. Notably, the RGMA-MSCs display superior electrochemical properties, including exceptionally high rate capability (up to 50000 mV·s^{-1}), high frequency response (very short corresponding time constant $\tau_0 = 0.14$ ms), and excellent cycle stability (90.3% of the initial capacitance after 6000 cycles in ionic liquid gel electrolyte). Importantly, the electrochemical performance of RGMA-MSCs shows a strong dependence on the geometric parameters including the interspace between adjacent fingers and the width of the finger of MSCs. These encouraging results may not only provide important references for the design and fabrication of high-performance MSCs, but also make the RGMA ternary hybrid film promising for the next generation film lithium ion batteries and other energy storage devices.

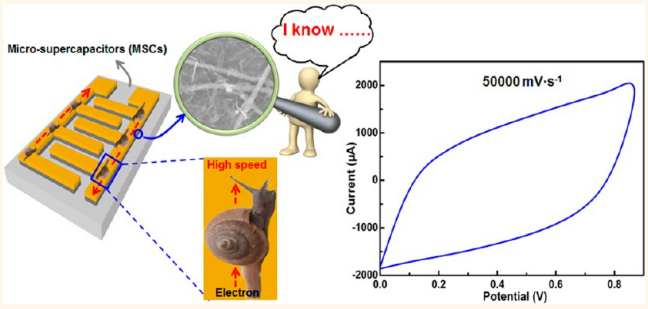

KEYWORDS: microsupercapacitors · reduced graphene oxide · MnO_2 · sliver nanowire · hybrid film

The rapid development of wireless sensor networks, portable electronic devices, and other self-powered microsystems has significantly increased the demand for microelectrochemical energy storage devices.[1−7] Meanwhile, considering the demand of miniaturization and reduction of the complexity of the whole system, the design and fabrication of efficient, miniaturized energy-storage devices with long lifetime, high rate capability, and high energy delivery is of great significance.

Microsupercapacitors (MSCs), a novel class of micro/nanoscale power source, have attracted considerable attention because of their unique features, such as an ultrahigh power density compared with that of batteries, large rate capability, long cycling lifetime, and being environmental friendly.[6−11] Moreover, MSCs can be directly coupled with other energy storage units (microbatteries and fuel cell), microsensors, and biomedical implants to offer sufficient peak power.[12−14] Therefore, a great deal of attention has been focused on planar MSCs, for which a series of nanostructured active materials have been developed.[15−32] Among them, graphene-based materials, such as graphene,[33] reduced graphene oxide,[7,9,10,18,34] graphene quantum dots,[35] graphene/CNTs,[36−38] graphene/polyaniline,[39] and graphene/MnO_2,[40] have been exploited as active materials for planar MSCs by taking advantage of the unique properties of graphene and the synergistic effect between graphene and the other component. However, the relatively low electrical

* Address correspondence to ebktay@ntu.edu.sg.

Received for review October 23, 2014 and accepted January 5, 2015.

Published online January 05, 2015
10.1021/nn5060442

conductivities of graphene-based films derived from graphite oxide limit their superior performances to some extent,[41] because the electrical properties of intrinsic graphene are difficult to completely recover after reduction due to the presence of domain boundaries, defect, and residual oxygen-containing functional groups for chemically exfoliated graphene sheets.[41] Additionally, a larger number of contact resistances between small-size graphene sheets also drastically degrade their electrical transport properties. Thus, how to reasonably design and prepare the highly conductive and flexible graphene-based films with low cost and facile preparation processes is still a challenge for the high-performance MSCs and other energy storage devices.

To address the aforementioned problems, one effective strategy is to design and build a novel graphene-based nanostructured active material combining two energy storage mechanisms (electrical double layer capacitive and pseudocapacitive), highly accessible electrochemically activated surface area, high electrical conductivity, and superior interfacial integrity of the main components. To this end, we have designed and fabricated the reduced graphene oxide/MnO_2/silver nanowire (AgNW) ternary hybrid film (RGMA ternary hybrid film) used as the electrode material for MSCs based on the following reasons: (1) graphene oxide (GO) provide fertile opportunities for the construction of graphene-based nanocomposites due to the abundant oxygen-containing functional groups, and may also be a reliable material for the flexible energy storage devices attributable to its better mechanical strength and stiffness; (2) MnO_2 not only significantly enhances the capacitive performances due to the pseudocapacitive contribution, but also prevents the restacking and aggregation of the graphene nanosheets; (3) 1D AgNW plays a key role as the conducting bridge between the graphene sheets or/needle-like MnO_2 to enhance the electrical conductivity and mechanical flexibility of the film, and also acts as the "spacer" to prevent the aggregation of graphene nanosheets. On the basis of so many extraordinary properties mentioned above, it is expected that the RGMA ternary hybrid film will show superior capacitive performance as the active material for MSCs.

Additionally, it is well-known that the electrochemical performances of supercapacitors not only rely on the exploitation of high-capacity active materials, but also on the rational design of electrode architectures, especially for MSCs with a limited surface area. On the basis of this point, it is both necessary and important to optimize the geometry of the current collectors for a given electrode material and to consider the performances of the MSCs normalized to its footprint area. Furthermore, thorough understanding of the effects of electrode structure on the electrochemical performances of MSCs is beneficial to better design and fabricate the MSCs with superior performances. However, compared to the work on electrode materials of MSCs, little work has been done on the effects of the electrode structure on the electrochemical performances of MSCs.

In this work, the MSCs based on the novel RGMA ternary hybrid film (RGMA-MSCs) are designed and successfully fabricated. Interestingly, the electrochemical performances of RGMA-MSCs show a strong dependence on the interspace between adjacent fingers, and the width of the fingers of MSCs. Meanwhile, a flexible, transparent, all-solid state RMGA-MSC is built and its electrochemical performance in ionic liquid gel electrolyte is also investigated in depth. Encouragingly, the as-prepared RGMA-MSCs display excellent electrochemical properties, including excellent rate capability, very short corresponding time constant, and long cycle life. In addition, the strategy presented here can be extended to prepare other ternary hybrid films, which may be promising for the next generation of high-performance MSCs, lithium ion batteries, and other energy storage devices.

RESULTS AND DISCUSSION

The GO/MnO_2/AgNW (GMA) ternary hybrid film is prepared by a facile vacuum filtration of the resultant complex dispersion of GO, MnO_2, and AgNW suspension (Figure 1a). After the vacuum filtration, the cellulose acetate membrane surface is uniformly and intimately covered by the GMA ternary hybrid film, as shown in the digital photograph (Figure 1b). Next, the as-obtained GMA ternary hybrid film is used as the active material to design and build the MSCs, as presented in Figure 1c. Briefly, the cellulose acetate membrane with captured GMA ternary hybrid film is transferred onto an alumina substrate, and then the cellulose acetate membrane is dissolved to leave the GMA ternary hybrid film on the substrate. Subsequently, gold pattern with the designed device configuration is thermally evaporated onto the GMA ternary hybrid film through the homemade interdigital finger mask. Afterward, the resulting patterned Au layer acts as a protection mask to etch the exposed graphene by O_2 plasma, and the residual MnO_2 and AgNW are removed by HCl solution. Finally, a thermal-reduction of the GMA ternary hybrid film is carried out by annealing the device at 300 °C for 2 h under argon atmosphere.

SEM images of pristine RGO, needle-like MnO_2, AgNW, and RGMA ternary hybrid film are shown in Figure 2. Figure 2a represents the typical SEM image of graphene sheets with richly wrinkled structure, which is favorable for the diffusion of electrolyte into the inner area of the RGMA.[34] As presented in Figure 2b, MnO_2 exhibits needle-like morphology with diameters from 20 to 50 nm and lengths from 200 to 500 nm.

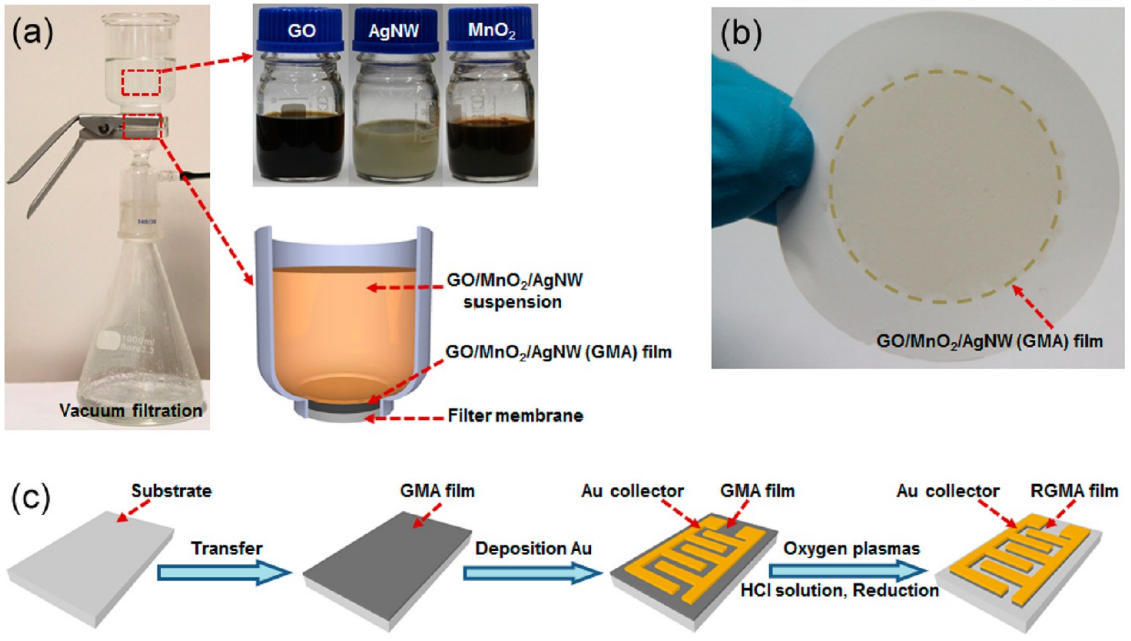

Figure 1. (a) Fabrication of the GMA ternary hybrid film through vacuum filtration of the mixture of GO, MnO_2, and AgNW suspension. (b) Digital photograph of the as-obtained GMA film supported on the cellulose acetate membrane after the vacuum filtration. (c) Schematic illustration of the fabrication procedures for RGMA-MSCs on an alumina substrate.

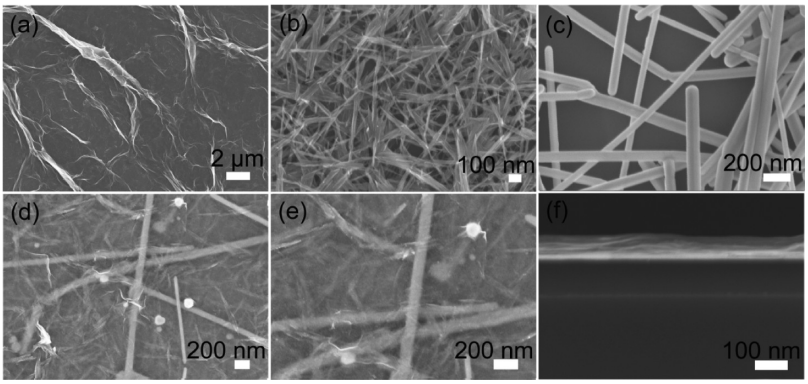

Figure 2. Top-view SEM images of (a) graphene, (b) needle-like MnO_2, (c) AgNW, and (d and e) RGMA ternary hybrid film. (f) Cross-sectional SEM image of RGMA ternary hybrid film on silicon wafer.

The diameters of AgNW (Figure 2c) range from 40 to 90 nm, and the lengths vary from several tens to hundreds of micrometers. Moreover, their corresponding TEM characterizations (Supporting Information Figure S1) further confirm the successful preparation of graphene sheets, needle-like MnO_2, and AgNW. As displayed in Supporting Information Figure S2, the low magnification SEM image of the top-view of the RGMA ternary hybrid film exhibits the smooth and flat morphology of in-plane structure. In this ternary hybrid film, graphene sheets, needle-like MnO_2, and AgNW are uniformly incorporated to form sandwiched structures through physisorption, electrostatic binding, or charge-transfer interactions.[42,43] The high magnification SEM images of the RGMA ternary hybrid film (Figure 2 panels d and e) clearly show that the randomly distributed 1D AgNWs are wrapped and soldered by the wrinkles and folds of the graphene sheets and that the needle-like MnO_2 are dispersed between the graphene sheets. In this unique structure, the graphene sheets with high surface area and high mechanical flexibility are beneficial to build a better conductive network which could promote the electron transfer. On the other hand, the needle-like MnO_2 and 1D AgNW can act as the "spacers" to prevent the restacking and aggregation of graphene nanosheets, and as a result, more electrolyte-accessible surface areas become available. Moreover, the inserted 1D AgNW can also act as a conductive bridge between the graphene sheets or/needle-like MnO_2 to provide effective electron-transport channels, further improving the conductivity of the hybrid film. As mentioned above, the RGMA ternary hybrid film may be a promising material for planar microsupercapacitors. Additionally, the layered structure of the RGMA ternary hybrid film can be clearly observed in the cross-sectional SEM image (Figure 2f)

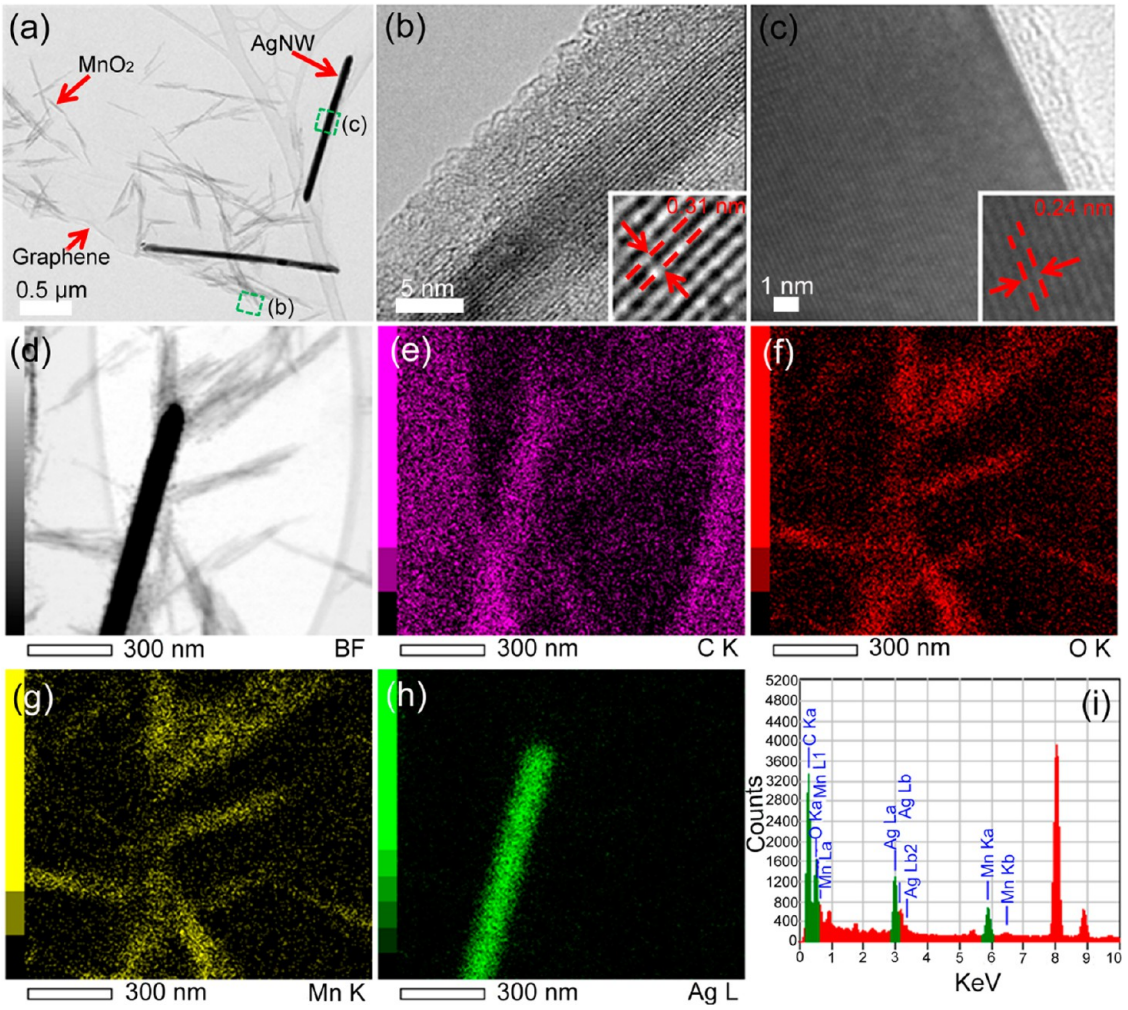

Figure 3. TEM images of the RGMA ternary hybrid film: (a) low-magnification micrograph, (b and c) HR-TEM image of the open square regions (green line) located in panel a, respectively. (d) HAADF-STEM image of the RGMA ternary hybrid film and the corresponding HAADF-STEM-EDS elemental mapping analysis of (e) C element mapping, (f) O element mapping, (g) Mn element mapping, and (h) Ag element mapping, respectively. (i) EDS spectrum of the RGMA ternary hybrid film.

with a thickness of about 60 nm (Supporting Information Figure S3), indicating the thin thickness of the ternary hybrid film.

More detailed structural information on the RGMA ternary hybrid film is investigated by transmission electron microscopy (TEM). Here, the TEM sample is prepared by a sonication process in ethanol, followed by casting them on the TEM copper grids. The typical TEM image of the RGMA ternary hybrid film (Figure 3a) reveals that the needle-like MnO_2 and the AgNW are well anchored on the surface of graphene sheets. HR-TEM images of the RGMA ternary hybrid film indicated by the green dotted square frame (Inset in Figure 3a) are shown in Figure 3 panels b and c, respectively. The distance between the adjacent lattice fringes that run parallel to the nanowire is around 0.30 nm (Figure 3b), which agrees well with the interplanar distance of the (001) plane of the α-MnO_2 structure.[44] As presented in Figure 3c, the clear lattice fringes with the measured interplanar spacing of 0.24 nm corresponds to the (110) of AgNW,[45] suggesting that the AgNW is single-crystalline with the (110) growth direction. Moreover, elemental mapping spectra show the presence and the distribution of the C, O, Mn, and Ag elements, as presented in Figure 3 panels e, f, g, and h, respectively, giving evidence to the successful preparation of a ternary hybrid film compounded from the RGO, needle-like MnO_2, and AgNW. Additionally, energy dispersive X-ray spectrometry (EDS) spectrum (Figure 3i) exhibits only peaks of C, O, Mn, and Ag except for the Cu signal originating from the copper grid, also supporting the incorporation of RGO, needle-like MnO_2, and AgNW in this ternary hybrid film.

XPS spectra are used to analyze the functionalities and the existence of covalent bonds in the RGMA ternary hybrid film in depth. The survey spectrum (Figure 4a) exhibits the presence of C, O, Mn, and Ag elements, deriving from the RGO, MnO_2, and AgNW in RGMA ternary hybrid film. The high resolution C 1s XPS spectrum (Figure 4b) of the RGMA ternary hybrid film can be fitted into four components associated with four different chemical environments of carbon atoms

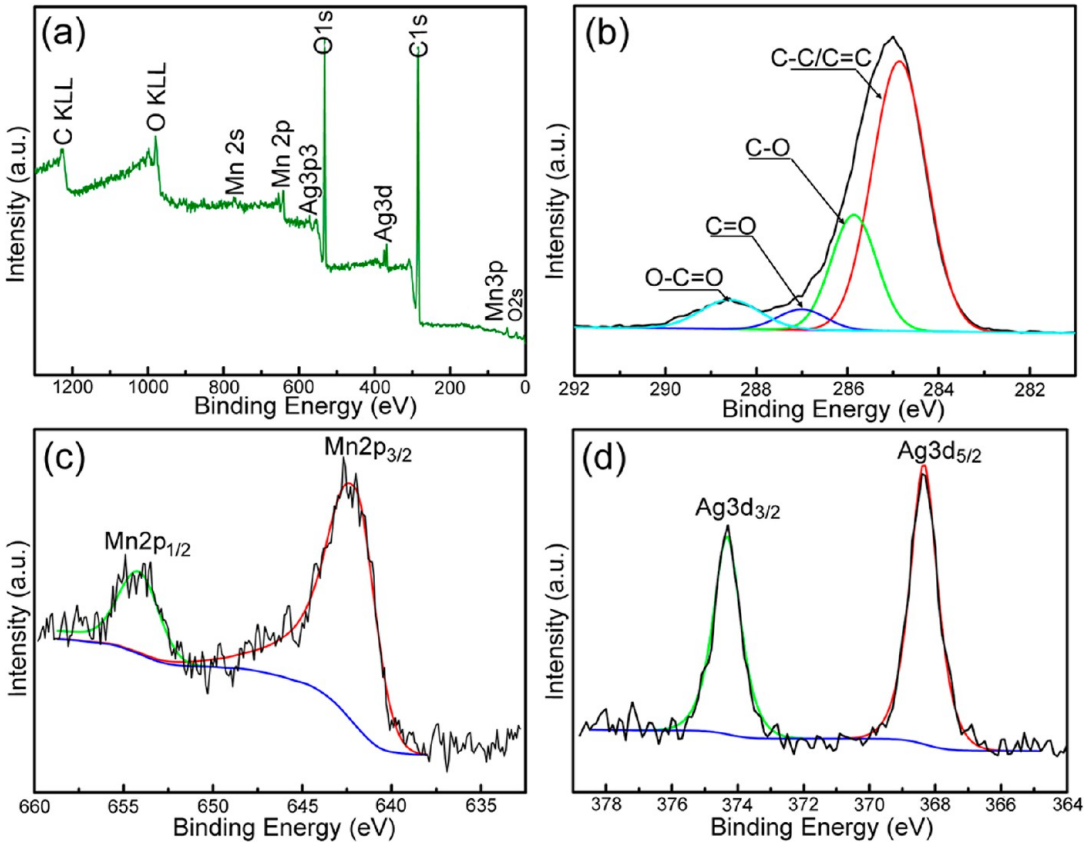

Figure 4. XPS spectra of the RGMA ternary hybrid film: (a) survey spectrum, (b) high-resolution C 1s spectrum, (c) high-resolution Mn 2p spectrum, and (d) high-resolution Ag 3d spectrum, respectively.

including nonoxygenated carbon (C−C/C═C, 284.8 eV), C in C−O bonds (285.9 eV), carbonyl carbon (C═O, 287.1 eV), and carboxylate carbon (O−C═O, 288.6 eV).[46,47] Compared with the C 1s XPS spectrum of GO (Supporting Information Figure S4), the significant intensity enhancement of nonoxygenated carbon and the decrease of oxygen-containing functionalities have demonstrated the efficient reduction of graphene oxide. As shown in Figure 4c, the appearance of two peaks centered at 642.3 and 654.4 eV can be assigned to Mn $2p_{3/2}$ and Mn $2p_{1/2}$, respectively, indicating that Mn mainly exists in the form of Mn^{4+} in RGMA ternary hybrid film, which correlates with previously reported data.[48,49] Obviously, the typical Ag 3d spectrum (Figure 4d) with two major peaks at 374.3 and 368.2 eV, corresponding to Ag $3d_{5/2}$ and Ag $3d_{3/2}$, respectively, reveals that the AgNW is present in the metallic state in a RGMA ternary hybrid film.[49,50] In addition, the results obtained by Raman and FT-IR spectroscopy (Supporting Information Figure S5) also confirm that the RGMA ternary hybrid film composed of RGO, MnO_2, and AgNW are successfully prepared by the facile vacuum filtration and subsequent thermal-reduction.

To evaluate the effects of the width of the interspace between the adjacent fingers on the electrochemical performances of RGMA-MSCs, RGMA-MSCs with different width of the interspace between the adjacent fingers (200 μm, 400 μm, and 800 μm) are fabricated on the same total surface of the cell (Figure 5), and the corresponding RGMA-MSCs are denoted as MSCs(WI200), MSCs(WI400), and MSCs(WI800), respectively. Here, except for the width of the interspace between the adjacent fingers, the other parameters such as the width of finger, the length of the finger, and the thickness of the RGMA ternary hybrid film are kept constant (Supporting Information Figure S6). Cyclic voltammetry (CV) measurements recorded at scan rates from 10 to 50000 $mV \cdot s^{-1}$ are performed to reveal the effect of the width of interspace between the adjacent fingers on the electrochemical performances of as-made RGMA-MSCs. All CV curves of the RGMA-MSCs (Figure 6 panels a, b, and c) present the nearly rectangular shape and rapid current response on voltage reversal at each potential, confirming the formation of an efficient electric double layer and fast charge/discharge propagation within the RGMA ternary hybrid film.[10,35,40,48] Even at an ultrahigh scan rate of 50000 $mV \cdot s^{-1}$, the CV curve still remains in a rectangular shape, suggesting the high-power capability of RGMA-MSCs.[29,35,40] Such high rate performance of RGMA-MSCs is comparable to that of the high-power MSCs based on other nanomaterial, including carbide-derived carbon,[28] onion-like carbon,[13] reduced graphene oxide,[7,9,10,18,34] graphene quantum dots,[35]

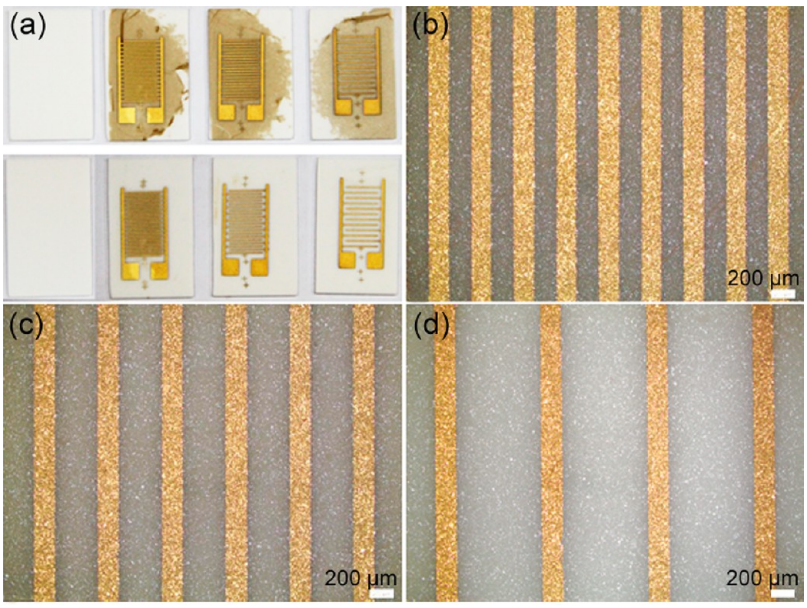

Figure 5. (a) Digital photography of RGMA-MSCs with different widths of the interspace between the adjacent fingers after the deposition of Au current collectors (top) and the subsequent treatment by O_2 plasma (bottom). Optical images of (b) MSCs(WI200), (c) MSCs(WI400), and (d) MSCs(WI800), respectively.

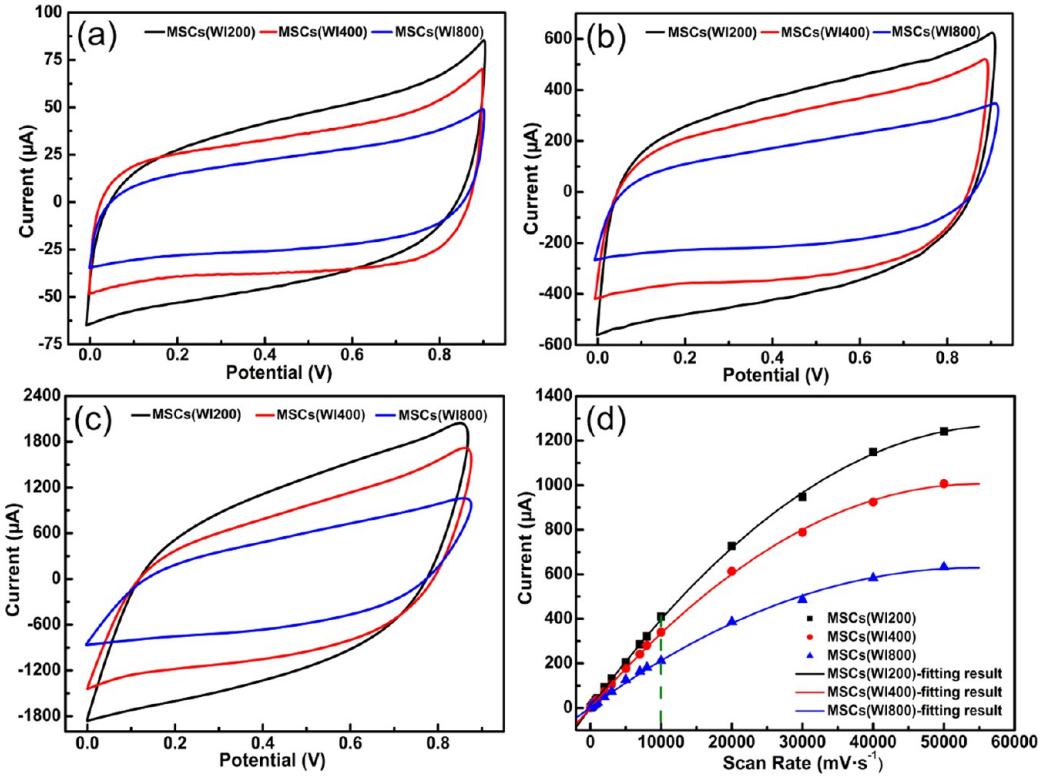

Figure 6. CV curves of MSCs(WI200), MSCs(WI400), and MSCs(WI800) with different width of the interspace between the adjacent fingers at different scan rates: (a) 1000 mV·s^{-1}, (b) 10000 mV·s^{-1}, (c) 50000 mV·s^{-1}, respectively. (d) Evolution of the corresponding discharge current *versus* scan rate for MSCs(WI200), MSCs(WI400), and MSCs(WI800), respectively. A linear dependence is obtained up to at least 10000 mV·s^{-1} (green dash dot line), indicating an ultrahigh power ability for the MSCs.

graphene/CNTs,[36−38] graphene/polyaniline,[39] and graphene/MnO_2.[40] Here, the absence of redox peaks on the CV curves indicates that RGMA-MSCs are charged/discharged at a pseudoconstant rate over the entire voltammetric cycles.[51] Moreover, we plot the discharge current of RGMA-MSCs with a different width of the interspace between the adjacent fingers as a function of the scan rates from 10 to 50000 mV·s^{-1} (Figure 6d). Obviously, the discharge current values of RGMA-MSCs show a linear dependence on scan rates

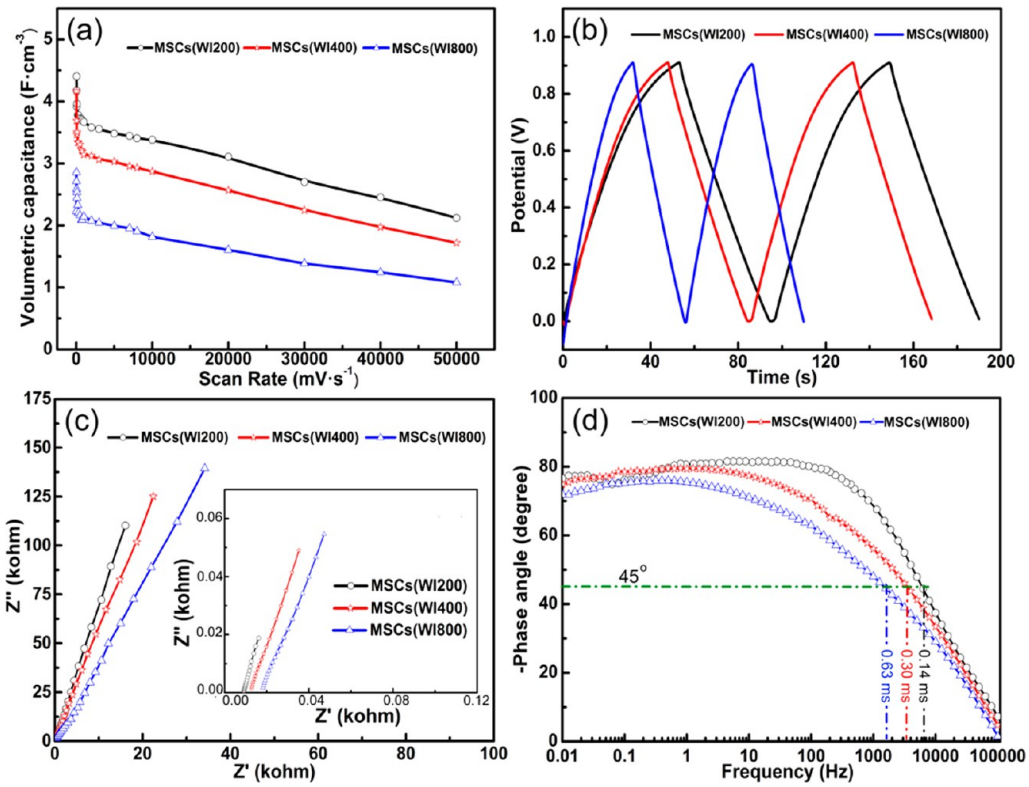

Figure 7. Electrochemical performances of MSCs(WI200), MSCs(WI400), and MSCs(WI800) with different width of the interspace between the adjacent fingers: (a) Evolution of the stack capacitance *versus* scan rate, (b) galvanostatic charge/discharge curves at a fixed current density of 85 mA·cm^{-2}, (c) complex plane plot of the impedance spectrum (inset is a magnified plot of the high-frequency region), and (d) impedance phase angle as a function of frequency ranging from 100 kHz to 10 mHz. The frequency at the 45° phase angle reveals the power capability of the MSCs.

from 10 to 10000 mV·s^{-1}, but the current values slowly deviate from the linear region when the scan rates exceed 10000 mV·s^{-1}, probably owing to the limited ion diffusion at ultrahigh scan rates.[6,7,9,29,52−56] Notably, at a fixed scan rate, the narrower the width of interspace is between the adjacent fingers in the RGMA-MSCs, the larger are the discharge current responses, because decreasing the width of interspace between the adjacent fingers efficiently decreases the average ionic diffusion pathway between the adjacent fingers and consequently decreases the electrolyte resistance.[30,34]

To better understand the effects of the width of interspace between the adjacent fingers on the electrochemical performances of RGMA-MSCs, the volumetric specific capacitance, the galvanostatic charge/discharge curves, and electrochemical impedance spectroscopy are shown in Figure 7. Recently, it was reported that the volumetric capacitances give a more accurate picture of the true performance of a supercapacitor compared with gravimetric values,[29,35,36,57] especially for the MSCs because of the small mass of the active material. Therefore, the specific capacitance of the MSCs is calculated based on the volume of the stack, if not otherwise specified. Figure 7a plots the volumetric specific capacitance (F·cm^{-3}) of the RGMA-MSCs as a function of scan rate ranging from 10 to 50000 mV·s^{-1}. Clearly, the volumetric specific capacitances of the RGMA-MSCs decrease with the increase of scan rates, which is attributed to the insufficient time available for ion diffusion and adsorption in the inner of the electrode materials at a very high scan rate.[32,34,58] Interestingly, the larger is the width of the interspace between the adjacent fingers, the smaller is the volumetric specific capacitance that can be extracted from the RGMA-MSCs at various scan rates, which is mainly attributed to the different pathway for ion diffusion from the bulk solution to the electrode surface. The greater width of the interspace between the adjacent fingers results in the longer ionic diffusion pathway between two microelectrodes. Therefore, the highest specific capacitance of the MSCs(WI200) is recorded to be 4.42 F·cm^{-3} at a scan rate of 10 mV·s^{-1}. The present value is comparable with the values of other reported materials for MSCs such as onion-like carbon (1.10 F·cm^{-3}),[13] graphene/CNTs (1.08 F·cm^{-3}),[37] laser reduction graphene (3.10 F·cm^{-3}),[10] active carbon (9.00 F·cm^{-3}),[13] and reduced graphene film (17.5 F·cm^{-3}).[9] Here, the enhanced capacitance of RGMA-MSCs is mainly contributed by the RGMA ternary hybrid film due to its unique structure and the synergistic effect of each component, which can be strongly supported by the data in Supporting Information Figure S7. As displayed in

Figure 7b, all charge/discharge curves of RGMA-MSCs show nearly ideal triangular shape and no obvious voltage drop observed at the beginning of each discharge, indicating ideal capacitor behavior and the very low resistance for all of the RMGA-MSCs.[29,35,48,52] Furthermore, the discharge time of the RMGA-MSCs decreases as the width of interspace between the adjacent fingers increases, suggesting that increasing the width of interspace between the adjacent fingers leads to the decrease of specific capacitance of the RMGA-MSCs. The results from charge/discharge curves are in good agreement with the CV results in terms of specific capacitance of the RMGA-MSCs. Additionally, the self-discharge behavior of the RGMA-MSCs is also measured. As presented in Supporting Information Figure S8, self-discharge curves of the RGMA-MSCs reveal the relatively long self-discharge time (from V_{max} to $^1/_2V_{max}$),[10,12,19,32] indicating low self-discharge characteristics, which endow them with high potential for practical applications.

Electrochemical impedance spectra of the RMGA-MSCs with different width of the interspace between the adjacent fingers are presented in Figure 7c. Complex plane plots of RMGA-MSCs exhibit the closed 90° slope at a low frequency, which is another characteristic of the ideal capacitive behavior of RMGA-MSCs.[9,21,35,48] The more vertical is the line, the more closely the RGMA-MSCs behaves as an ideal capacitor.[36,59,60] Moreover, all RMGA-MSCs show the near-vertical line intersection with the real axis at high frequency (inset in Figure 7c), indicative of the small equivalent series resistance due to the fast ion diffusion. In contrast, RGMA-MSCs(WI200) exhibits the smallest equivalent series resistance, attributable to the shortest ion diffusion pathway resulting from the narrowest width of interspace between the adjacent fingers. For a more informative analysis of EIS test, the dependence of the phase angle on the frequency for RMGA-MSCs with different width of the interspace between the adjacent fingers is shown in Figure 7d. For frequencies up to 10 Hz, all phase angles of the RMGA-MSCs are close to 90°, which indicates that these device functionalities are close to those of the ideal capacitors,[9,18,52] coinciding with the *RC* (a serial resistance *R* and capacitance *C*) equivalent circuit.[35,48] A better comparison of the frequency response of the RMGA-MSCs can be made by comparing the characteristic frequency (f_0) at the phase angle of 45°.[9,13,35,36,48,54] It is observed that the characteristic frequency is 7142 Hz for RGMA-MSCs(WI200), much higher than 3334 Hz for RGMA-MSCs(WI400), and 1587 Hz for RGMA-MSCs(WI800). Therefore, the corresponding time constant τ_0 ($\tau_0 = 1/f_0$), the minimum time needed to discharge all the energy from the device with an efficiency of more than 50%,[9,13,18,35,36,48,52,54] is 0.14 ms for RGMA-MSCs(WI200), in contrast to 0.30 ms for RGMA-MSCs(WI400) and 0.63 ms for RGMA-MSCs(WI800). Importantly, the time constants for the RGMA-MSCs are very promising compared with previously reported values for MSCs such as activated carbon (700 ms),[13] onion-like carbon (26 ms),[13] laser reduction graphene (19 ms),[10] graphene/CNT composite (3.4 ms),[36] and reduced graphene film (0.28 ms).[9] The small time constants reveal the excellent power response of the RGMA-MSCs. On the basis of the above-mentioned results, it can be reasonably concluded that for a given total area, the narrower is the width of the interspace between the adjacent fingers, the better is the rate capability, the faster is the power response, and the higher is the energy the RGMA-MSCs possess. Furthermore, these results also demonstrate that the RGMA ternary hybrid film possesses superior characteristics compared to the reported materials and can be a very promising active material for MSCs.

In addition to the width of interspace between the adjacent fingers, the effects of the width of finger on the electrochemical performances of RGMA-MSCs are also investigated in this work in depth. RGMA-MSCs with the different widths of finger (200 μm, 400 μm, and 800 μm) are fabricated on the same total surface of the cell (Figure 8), and the corresponding microsupercapacitors are denoted as MSCs(WF200), MSCs(WF400), and MSCs(WF800). Herein, other parameters (including the width of interspace between the adjacent fingers, the length of the finger, and the thickness of the RGMA ternary hybrid film) are kept constant except for the width of finger (Supporting Information Figure S9). The CV curves of RGMA-MSCs with the different width of finger at different scan rates are shown in Figure 9 panels a, b, and c, respectively. Obviously, even at a very high scan rate of 50000 mV·s^{-1}, the CV curves only slightly deviate from the rectangular shape, indicating the nearly ideal capacitive behavior and the high power output capability of RGMA-MSCs.[18,29,35,40,52,53] Notably, with the increase of the width of the finger, the area surrounded by the CV curves of RGMA-MSCs decreases, suggesting that the MSCs(WF200) has the largest current response, and further revealing the influence of the width of finger on the specific capacitance of RGMA-MSCs. The in-depth study of the relationship between the current response and the scan rate is presented in Figure 9d. Remarkably, a linear dependence of the discharge current on the scan rate is recognized at least up to 10000 mV·s^{-1}, indicating the characteristic of a high instantaneous power. Such rate performance is better than or comparable to those of the high-power MSCs previously reported.[10,13,28,35−40] However, when the scan rate further increases up to 50000 mV·s^{-1}, the discharge current shows the nonlinear dependence on the scan rate, revealing the diffusion-controlled mechanism.[29,54]

To highlight the effects of the width of finger on the electrochemical performances of RGMA-MSCs, the

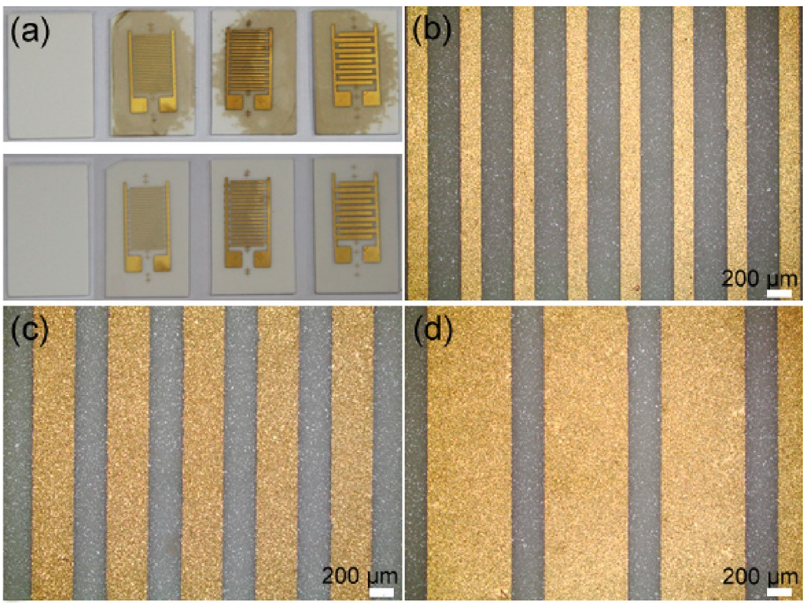

Figure 8. (a) Digital photography of RGMA-MSCs with different widths of the fingers after the deposition of Au current collectors (top) and the subsequent treatment by O_2 plasma (bottom). Optical images of (b) MSCs(WF200), (c) MSCs(WF400), and (d) MSCs(WF800), respectively.

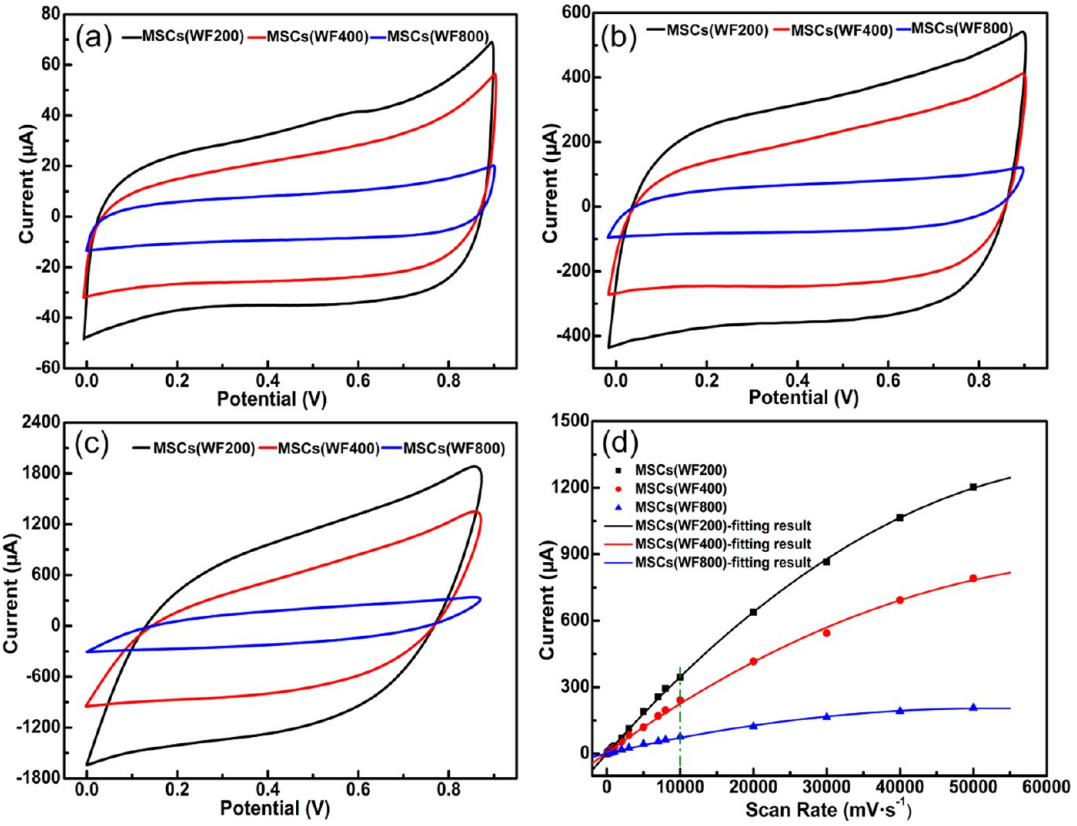

Figure 9. CV curves of MSCs(WF200), MSCs(WF400), and MSCs(WF800) with different widths of fingers at different scan rates: (a) 1000 mV·s^{-1}, (b) 10000 mV·s^{-1}, (c) 50000 mV·s^{-1}, respectively. (d) Evolution of the corresponding discharge current *versus* scan rate for MSCs(WF200), MSCs(WF400), and MSCs(WF800), respectively. A linear dependence is obtained up to at least 10000 mV·s^{-1} (green dash dot line), indicating an ultrahigh power ability for the MSCs.

volumetric specific capacitance, the galvanostatic charge/discharge curves, and electrochemical impedance spectroscopy (EIS) are also performed. The volumetric specific capacitances are plotted as a function of scan rates ranging from 10 to 50000 mV·s^{-1}, as displayed in Figure 10a. It shows that the volumetric specific capacitance decreases with the increase of scan rate from 10 to 50000 mV·s^{-1}, which is attributed to the

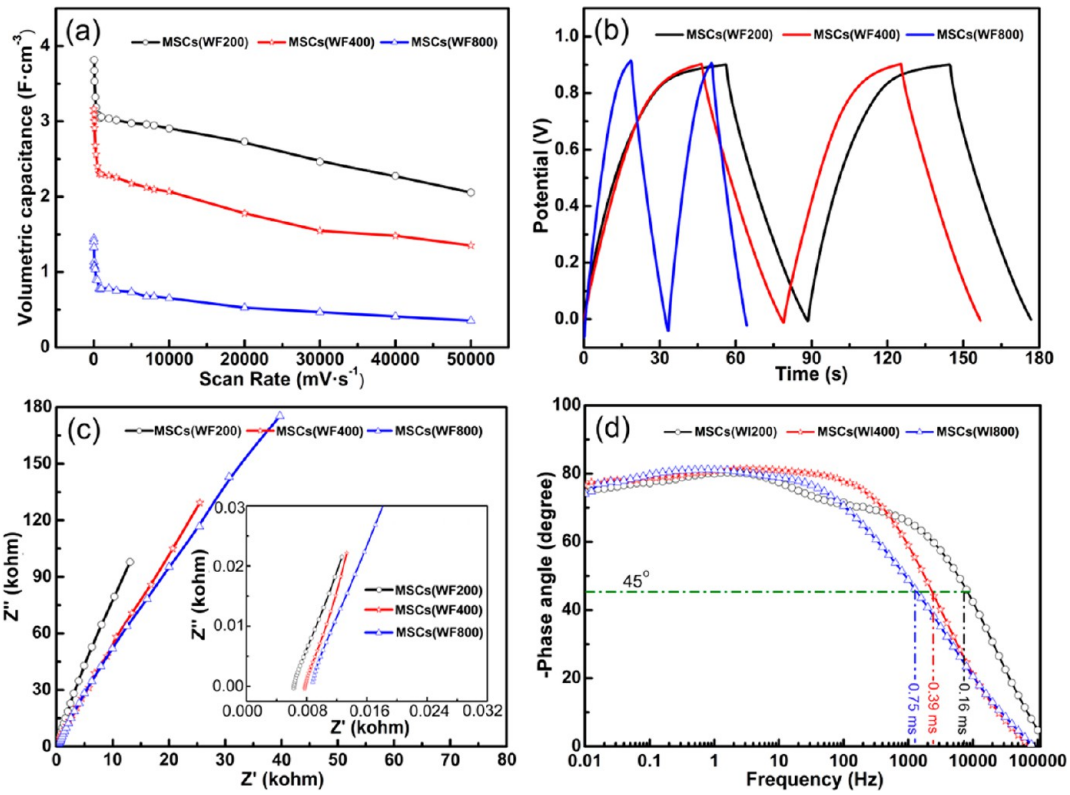

Figure 10. Electrochemical performances of MSCs(WF200), MSCs(WF400), and MSCs(WF800) with different widths of the finger: (a) evolution of the stack capacitance *versus* scan rate, (b) charge/discharge curves at a fixed current density of 85 mA·cm^{-2}, (c) complex plane plot of the impedance spectrum (inset is a magnified plot of the high-frequency region), and (d) impedance phase angle as a function of frequency ranging from 100 kHz to 10 mHz. The frequency at the 45° phase angle reveals the power capability of the MSCs.

diffusion effect causing some active surface areas to be inaccessible for charge storage.[32,34,61] Importantly, the volumetric specific capacitances of RGMA-MSCs show a downward trend with the increase of the width of finger, demonstrating that for a given total area, the narrower is the width of the finger, the larger is the volumetric specific capacitance of RGMA-MSCs. This is because narrowing the finger width efficiently decreases the ionic diffusion pathway in the inner area of the electrode materials, and consequently decreases the resistance due to the ion transport limitations.[7,10,34] Moreover, the narrower finger maximizes the available electrochemical surface area and results in the increased capacitance observed with the RGMA-MSCs. Here, these capacitances are comparable with those of MSCs using other active materials.[9,10,13,37] The effect of the width of finger on the electrochemical performances of the RGMA-MSCs is further revealed by the galvanostatic charge/discharge curves (Figure 10b). Notably, all the microdevices, regardless of the width of the finger, show nearly ideal triangular charge/discharge curves, but increasing the width of finger results in the decrease of discharge time at a given current density, which is consistent with the aforementioned results obtained from the CV curves.

As shown in Figure 10c, the Nyquist plot of the RGMA-MSCs nearly parallels the imaginary axis at the low frequency region, indicating pure capacitive behavior related to the charge/discharge mechanism of the RGMA ternary hybrid film. Also, the plot does not show a semicircle at the high frequency region, implying the fast charge transfer in the RGMA ternary hybrid film.[35] Figure 10d presents the phase angles of these RGMA-MSCs close to 90° at the frequency of 10 Hz, revealing another typical characteristic of the ideal capacitor behavior.[9,18,35,48,52] Moreover, the RGMA-MSCs show superior frequency response with an extremely small relaxation time. The *RC* time constant of MSCs (WF200) is calculated to be 0.16 ms, in comparison to 0.39 ms for the MSCs (WF400) and 0.75 ms for the MSCs (WF800), indicating that the *RC* time constant of RGMA-MSCs decrease with the increase of the width of finger.

For application consideration, flexible and portable electronics may require highly flexible power sources. However, the fabrication of MSCs on a flexible substrate with good durability such as bending or twisting is still a challenge.[62] Therefore, we further adapt our fabrication method to construct flexible, transparent all-solid state MSCs on a polyethylene terephthalate (PET) substrate. Except for the substrate and the reduction method, the fabrication processes of RGMA-MSCs on a PET substrate, including transfer, deposition Au current collectors, and oxygen plasma etching, are

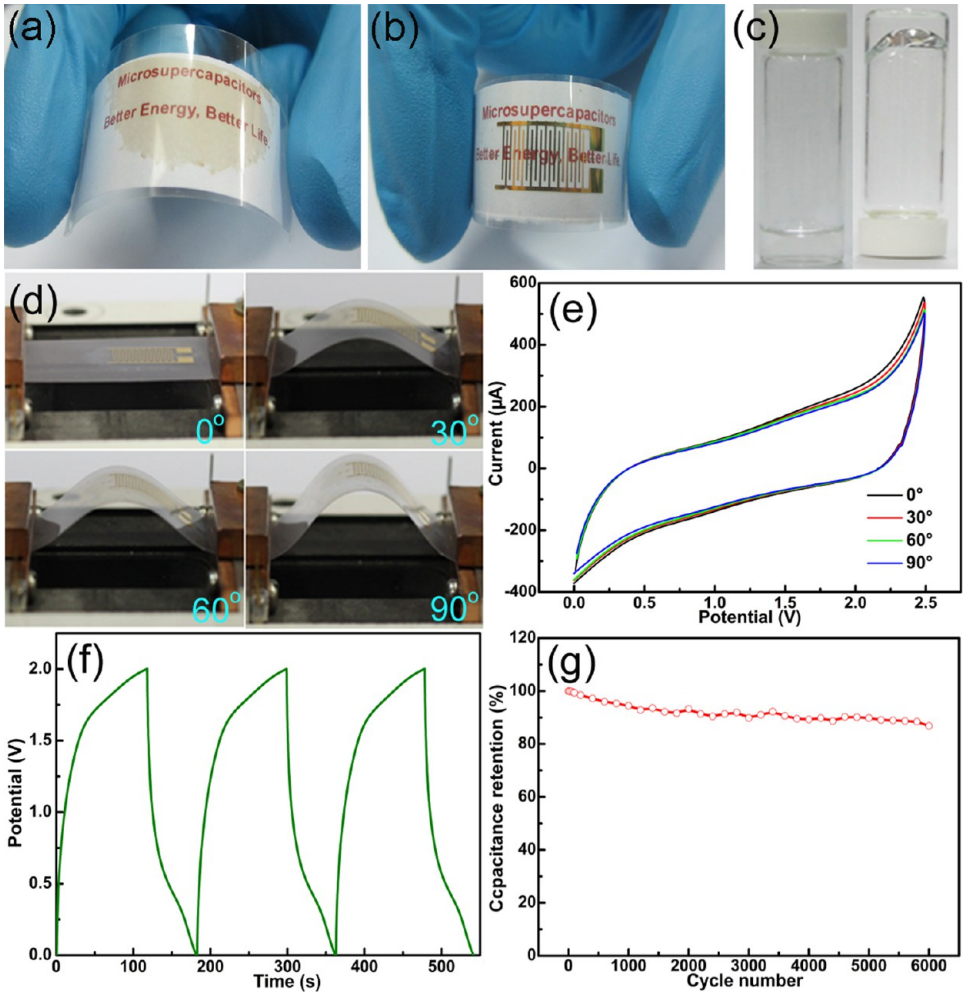

Figure 11. (a) Digital photograph of the as-fabricated RGMA ternary hybrid film transferred onto the PET substrate. (b) The resulting PET-supported RGMA-MSCs, showing the flexible and transparent characteristics of the as-prepared MSCs. (c) Digital photograph of the as-prepared ionic liquid gel electrolyte used in the assembly of the PET-supported RGMA-MSCs. (d) Optical images of PET-supported RGMA-MSCs bended with different angles. (e) CV curves of PET-supported RGMA-MSCs bended with different angles at the scan rate of 5000 mV·s^{-1}. (f) Galvanostatic charge/discharge curves of PET-supported RGMA-MSCs at a current density of 85 mA·cm^{-3}. (g) Specific capacitance of PET-supported RGMA-MSCs as a function of cycle number in ionic liquid gel electrolyte at 5000 mV·s^{-1}.

the same as for RGMA-MSCs on an aluminum substrate (see details in Methods). A RGMA ternary hybrid film on the bent PET substrate (Figure 11a) positioned above shows the features of large-area uniformity, good transparency, and mechanical flexibility. The optical image of typical PET-supported RGMA-MSCs is shown in Figure 11b.

Many efforts have been devoted to build the all-solid-state MSCs using aqueous hydrogel-polymer electrolytes, but the narrow operating voltage (no more than 1.0 V) of the devices strongly limits their applications due to the low decomposition voltage of water. Fortunately, compared with the water-based electrolytes, ionic liquids provide an attractive alternative to these conventional electrolytes owing to their wide electrochemical window, high ionic conductivity, and excellent electrochemical stability.[10,18,63] Therefore, it can be expected that the combination of ionic liquids with a solid matrix not only retain the excellent properties of ionic liquids, but also allow easy shaping of the device without having the intrinsic leakage problems of liquid electrolyte. Herein, we prepare a new ionic liquids-based gel (Figure 11c) by mixing together fumed silica nanopowder with the 1-butyl-3-methylimidazolium bis(trifluoromethylsulfonyl)imide.[10]

The electrochemical performances of RGMA-MSCs in ionic liquid gel electrolyte are shown in the Supporting Information Figure S10. Note that the CV curves remain nearly rectangular in shape even at an ultrahigh scan rate of 10000 mV·s^{-1}, indicating good capacitor behavior and excellent rate capability. Importantly, compared with the aqueous electrolyte, RGMA-MSCs operate at a larger potential window ranging from 0 to 2.5 V in an ionic liquid gel electrolyte, and thus are beneficial to achieving higher energy densities. The effect of curvature on the performances of the PET-supported RGMA-MSCs is examined by CV curves with the potential window ranging from 0 to 2.5 V at a scan

rate of 5000 $mV \cdot s^{-1}$ under four different bending angles (0°, 30°, 60°, and 90°), as shown in Figure 11d. No apparent change of the CV curves of the PET-supported RGMA-MSCs when tested under four bending states are observed (Figure 11e), suggesting that the electrochemical performances of the PET-supported RGMA-MSCs are hardly affected by the bending angles. The galvanostatic charge/discharge curve of the flexible, transparent all-solid-state RGMA-MSCs is presented in Figure 11f. Both the near linear and symmetry profile of charge/discharge curves reveals the good capacitive characteristics of the flexible, transparent all-solid-state RGMA-MSCs in ionic liquid gel electrolyte.[35,52] It shows a specific capacitance of 2.72 $F \cdot cm^{-3}$ at a current density of 85 $mA \cdot cm^{-3}$. In addition, the long-term cycling stability of the flexible, transparent all-solid-state RGMA-MSCs is also tested through a repetitive CV cycle at a scan rate of 5000 $mV \cdot s^{-1}$ (Figure 11g). Encouragingly, the flexible, transparent all-solid-state RGMA-MSCs still remain at 90.3% of the initial capacitance after 6000 cycles, demonstrating its excellent long-term cycling stability in an ionic liquid gel electrolyte.

To further demonstrate the performances of RGMA-MSCs, a Ragone plot is shown in Supporting Information Figure S11. Remarkably, the RGMA-MSCs deliver the volumetric energy densities of 2.3 $mWh \cdot cm^{-3}$ (power density of 162.0 $mW \cdot cm^{-3}$) in an ionic liquid gel electrolyte and 0.45 $mWh \cdot cm^{-3}$ (power density of 89.1 $mW \cdot cm^{-3}$) in a Na_2SO_4 electrolyte, which are comparable to or higher than those of recently reported microsupercapacitors based on other materials, including laser-scribed graphene,[10,18] reduced graphene oxide and carbon nanotube composites,[36] 3-dimensional graphene/carbon nanotube carpets,[37] laser scribed graphene/carbon nanotubes,[38] and photoresist derived porous carbon.[67] Encouragingly, these energy density values are at least 2 orders of magnitude higher than those of commercial electrolytic capacitors (3 V/300 μF),[10,18] and even comparable to those of the thin-film lithium battery (4 V/500 μAh).[13] The above results demonstrate that the RGMA-MSCs have excellent electrochemical performances with simultaneously high energy density and power density. Therefore, it can be expected that these superior energy and power performances of the RGMA-MSCs presented here could enable them to compete with microbatteries and electrolytic capacitors in a variety of applications.

CONCLUSION

In summary, we have demonstrated a simple efficient vacuum filtration method for constructing large-area, ultrathin, uniform GO/MnO_2/AgNW ternary hybrid films, which may provide the opportunity to incorporate metal or metal oxide nanostructures into doped-graphene film with great potential for other thin-film energy storage and conversion devices. More importantly, the electrochemical performances of the fabricated MSCs based on reduced graphene oxide/MnO_2/AgNW (RGMA) ternary hybrid film exhibit a strong dependence on the width of the interspace between the fingers and the width of finger, which presents important references for the design and fabrication of novel high-performance MSCs. Furthermore, the as-fabricated RGMA ternary hybrid film can be easily transferred onto transparent and flexible substrates to build the transparent, flexible, all-solid-state MSCs which demonstrate excellent electrochemical performance including high energy and power densities, robust lifetime cycling performance, and high flexibility. Therefore, the RGMA ternary hybrid film holds promise for the fabrication of next-generation high performance transparent, flexible, energy storage devices such as flexible lithium ion batteries.

METHODS

Synthesis of Graphene Oxide (GO), AgNW and Needle-like MnO_2. GO nanosheets were prepared from natural graphite (325 mesh) by a modified Hummers method.[64] AgNW was synthesized by a solvothermal process according to the reported method.[65] Needle-like MnO_2 was fabricated by a refluxing method as described previously.[66]

Preparation of GO/MnO_2/AgNW (GMA) Ternary Hybrid Film. A 0.5 mL sample of aqueous suspension of GO nanosheets (0.1 $mg \cdot ml^{-1}$), 0.5 mL of aqueous suspension of MnO_2 (0.1 $mg \cdot ml^{-1}$), and 0.5 mL of aqueous suspension of AgNW (0.1 $mg \cdot ml^{-1}$) were mixed evenly, and then diluted with deionized water. Subsequently, the resulting suspensions were vacuum-filtrated using a Millipore filter (50 mm in diameter and 0.45 μm in pore size). Next, the cellulose acetate filter membrane with captured GMA ternary hybrid film was cut into the size of choice, and then transferred onto an alumina substrate using isopropyl alcohol to remove the trapped air between the hybrid film and the substrate. After that, the cellulose filter membrane was dissolved using acetone to leave a GMA ternary hybrid film on the alumina substrate. Finally, the hybrid film was rinsed with deionized water and dried at room temperature.

Fabrication of RGMA-MSCs Devices. Gold with a thickness of 25 nm was thermally evaporated onto the GMA ternary hybrid film through the homemade interdigital finger mask. The patterns of GMA microelectrodes on alumina substrate were then created by oxidative etching of the exposed graphene oxide by O_2 plasma for 7 min. Thereafter, the device was put into HCl solution (10%) at 75 °C for 10 s to remove the residual MnO_2 and AgNW, and then rinsed with deionized water. Finally, a thermal-reduction of GMA ternary hybrid film was carried out by annealing the device at 300 °C for 2 h under an argon atmosphere. In parallel, the flexible, transparent and solid-state flexible MSCs were fabricated on PET substrate except for the reduction of GO with hydrazine hydrate.

Morphology and Structural Characterization. A field emission scanning electron microscope (FESEM, LEO 1550 GEMINI) was employed to study the morphology of the as-prepared samples. Transmission electron microscopy (TEM), high resolution TEM (HRTEM), and energy-dispersive X-ray spectroscopy (EDX) mapping were carried out using a JEOL JEM-2100F. XPS experiments were performed on a Kratos photoelectron spectroscopy system equipped with an Al Kα monochromator X-ray source operating at a power of 350 W. Raman spectra were obtained

using a WITec CRM200 Raman system and the 532 nm line of an argon ion laser was used as the excitation source in all the measurements. Infrared spectra were recorded on an IRPrestige-21 by using pressed KBr pellets. The thickness of the hybrid film was determined on a Bruker Dektak XT surface profiler.

Electrochemical Characterization. All electrochemical measurements were carried out in a two-electrode system using an Autolab workstation (PGSTAT302N) at room temperature. The cyclic voltammetry (CV) tests were measured at different scan rates varying from 10 to 50000 $mV \cdot s^{-1}$ with the potential window from 0 to 0.9 V for 0.5 M Na_2SO_4 electrolyte and from 0 to 2.5 V for ionic liquid gel electrolyte, respectively. Galvanostatic charge/discharge tests were measured with the constant current density of 85 $mA \cdot cm^{-3}$ in 0.5 M Na_2SO_4 electrolyte (from 0 to 0.9 V) and ionic liquid gel electrolyte (from 0 to 2.0 V), respectively. All electrochemical impedance spectroscopy (EIS) plots were tested in the frequency ranging from 100 kHz to 0.01 Hz at open circuit potential with an AC perturbation of 5 mV. The capacitance values were calculated from the CV curves by the equation:

$$C_{device} = \frac{1}{\nu \cdot (V_f - V_i)} \int_{V_i}^{V_f} I(V)\, dV \quad (1)$$

The specific capacitances were calculated based on the volume of the device stack according to the following equation:

$$C_{stack} = \frac{C_{device}}{V} \quad (2)$$

where ν was the scan rate ($mV \cdot s^{-1}$), V_f and V_i were the potential limits of the voltammetric curve, $I(V)$ was the voltammetric discharge current (A), C_{device} was the capacitance contribution from hybrid film ($F \cdot cm^{-2}$), and C_{stack} was the volumetric stack capacitance of device ($F \cdot cm^{-3}$). The volumetric stack capacitances were calculated by taking into account the whole volume of the device, including the volume of hybrid film electrodes, the interspaces between the electrodes, and Au current collectors.

Additionally, the energy density (E) and power density (P) are calculated by the following equations, respectively:

$$E = \frac{C_{stack} \times \Delta V^2}{7200} \quad (3)$$

$$P = \frac{E \times 3600}{t} \quad (4)$$

where C_{stack} was the volumetric stack capacitance ($F \cdot cm^{-3}$), ΔV was the operating potential window (V), Δt was the discharge time (s), E was the energy density ($Wh \cdot cm^{-3}$), and P was the power density ($W \cdot cm^{-3}$).

Conflict of Interest: The authors declare no competing financial interest.

Acknowledgment. The authors thank Q. Zhang and Q. Luo for the help of electrochemical testing. The authors also acknowledge financial support from MOE Academic Research Fund (AcRF) RG81/12 project.

Supporting Information Available: Figures giving (1) TEM images and corresponding selected-area electronic diffraction (SAED) pattern of graphene, needle-like MnO_2, AgNW, respectively; (2) low-magnification SEM image of the top-view of the RGMA ternary hybrid film; (3) digital photograph of the as-prepared RGMA ternary hybrid film supported on a silicon substrate and the corresponding thickness; (4) XPS spectra of the GO; (5) Raman and FT-IR spectra of the RGO and the RGMA ternary hybrid film, respectively; (6) dimensions of the RGMA-based microsupercapacitors produced with the different interspaces between adjunct fingers of 200, 400, and 800 μm, respectively; (7) top-view SEM images of RGOs and digital photography of the microsupercapacitors, and CV curves of microsupercapacitors made of different materials at different scan rates; (8) self-discharge curves of (open-circuit potential *versus* time) of MSCs(WI200), MSCs(WI400), and MSCs(WI800) obtained immediately after precharged to V_{max} in the 0.5 M Na_2SO_4 electrolyte; (9) dimensions of the RGMA-based microsupercapacitors produced with the different widths of fingers of 200, 400, and 800 μm, respectively; (10) CV curves of RGMA-MSCs in ionic liquid gel electrolyte at different scan rates; (11) Ragone plots showing energy and power densities of RGMA-based microsupercapacitors in comparison to those of other microsupercapacitors and commercially available energy storage devices. This material is available free of charge *via* the Internet at http://pubs.acs.org.

REFERENCES AND NOTES

1. Simon, P.; Gogotsi, Y. Materials for Electrochemical Capacitors. *Nat. Mater.* **2008**, *7*, 845–854.
2. Rolison, D. R.; Long, J. W.; Lytle, J. C.; Fischer, A. E.; Rhodes, C. P.; McEvoy, T. M.; Bourg, M. E.; Lubers, A. M. Multifunctional 3D Nanoarchitectures for Energy Storage and Conversion. *Chem. Soc. Rev.* **2009**, *38*, 226–252.
3. Koo, M.; Park, K. I.; Lee, S. H.; Suh, M.; Jeon, D. Y.; Choi, J. W.; Kang, K.; Lee, K. J. Bendable Inorganic Thin-Film Battery for Fully Flexible Electronic Systems. *Nano Lett.* **2012**, *12*, 4810–4816.
4. Hu, L. B.; Choi, J. W.; Yang, Y.; Jeong, S.; La Mantia, F.; Cui, L. F.; Cui, Y. Highly Conductive Paper for Energy-Storage Devices. *Proc. Natl. Acad. Sci. U.S.A.* **2009**, *106*, 21490–21494.
5. Kaempgen, M.; Chan, C. K.; Ma, J.; Cui, Y.; Gruner, G. Printable Thin Film Supercapacitors Using Single-Walled Carbon Nanotubes. *Nano Lett.* **2009**, *9*, 1872–1876.
6. Wu, Z.-S.; Parvez, K.; Winter, A.; Vieker, H.; Liu, X. J.; Han, S.; Turchanin, A.; Feng, X. L.; Müllen, K. Layer-by-Layer Assembled Heteroatom-Doped Graphene Films with Ultrahigh Volumetric Capacitance and Rate Capability for Micro-Supercapacitors. *Adv. Mater.* **2014**, *26*, 4552–4558.
7. Wu, Z.-S.; Parvez, K.; Feng, X. L.; Müllen, K. Photolithographic Fabrication of High-Performance All-Solid-State Graphene-Based Planar Micro-supercapacitors with Different Interdigital Fingers. *J. Mater. Chem. A* **2014**, *2*, 8288–8293.
8. Sung, J. H.; Kim, S. J.; Jeong, S. H.; Kim, E. H.; Lee, K. H. Flexible Micro-supercapacitors. *J. Power Sources* **2006**, *162*, 1467–1470.
9. Wu, Z. S.; Parvez, K.; Feng, X. L.; Müllen, K. Graphene-Based in-Plane Micro-Supercapacitors with High Power and Energy Densities. *Nat. Commun.* **2013**, *4*, 2487–2494.
10. El-Kady, M. F.; Kaner, R. B. Scalable Fabrication of High-Power Graphene Micro-supercapacitors for Flexible and on-Chip Energy Storage. *Nat. Commun.* **2013**, *4*, 1475–1483.
11. Beidaghi, M.; Gogotsi, Y. Capacitive Energy Storage in Micro-scale Devices: Recent Advances in Design and Fabrication of Micro-supercapacitors. *Energy Environ. Sci.* **2014**, *7*, 867–884.
12. Gao, W.; Singh, N.; Song, L.; Liu, Z.; Reddy, A. L. M.; Ci, L. J.; Vajtai, R.; Zhang, Q.; Wei, B. Q.; Ajayan, P. M. Direct Laser Writing of Micro-supercapacitors on Hydrated Graphite Oxide Films. *Nat. Nanotechnol.* **2011**, *6*, 496–500.
13. Pech, D.; Brunet, M.; Durou, H.; Huang, P.; Mochalin, V.; Gogotsi, Y.; Taberna, P.-L.; Simon, P. Ultrahigh-Power Micrometre-Sized Supercapacitors Based on Onion-like Carbon. *Nat. Nanotechnol.* **2010**, *5*, 651–654.
14. Fu, Y. P.; Wu, H. W.; Ye, S. Y.; Cai, X.; Yu, X.; Hou, S. C.; Kafafy, H.; Zou, D. C. Integrated Power Fiber for Energy Conversion and Storage. *Energy Environ. Sci.* **2013**, *6*, 805–812.
15. Makino, S.; Yamauchi, Y.; Sugimoto, W. Synthesis of Electrodeposited Ordered Mesoporous RuO_x Using Lyotropic Liquid Crystal and Application toward Micro-supercapacitors. *J. Power Sources* **2013**, *227*, 153–160.
16. Xue, M. Q.; Xie, Z.; Zhang, L. S.; Ma, X. L.; Wu, X. L.; Guo, Y. G.; Song, W. G.; Li, Z. B.; Cao, T. B. Microfluidic Etching for Fabrication of Flexible and All-Solid-State Micro-supercapacitor Based on MnO_2 Nanoparticles. *Nanoscale* **2011**, *3*, 2703–2708.
17. Feng, J.; Sun, X.; Wu, C. Z.; Peng, L. L.; Lin, C. W.; Hu, S. L.; Yang, J. L.; Xie, Y. Metallic Few-Layered VS_2 Ultrathin

Nanosheets: High Two-Dimensional Conductivity for in-Plane Supercapacitors. *J. Am. Chem. Soc.* **2011**, *133*, 17832–17838.
18. El-Kady, M. F.; Strong, V.; Dubin, S.; Kaner, R. B. Laser Scribing of High-Performance and Flexible Graphene-Based Electrochemical Capacitors. *Science* **2012**, *335*, 1326–1330.
19. Meng, C.; Maeng, J.; John, S. W. M.; Irazoqui, P. P. Ultrasmall Integrated 3D Micro-Supercapacitors Solve Energy Storage for Miniature Devices. *Adv. Energy Mater.* **2014**, *4*, 1301269–1301275.
20. Pech, D.; Brunet, M.; Taberna, P. L.; Simon, P.; Fabre, N.; Mesnilgrente, F.; Conedera, V.; Durou, H. Elaboration of a Microstructured Inkjet-Printed Carbon Electrochemical Capacitor. *J. Power Sources* **2010**, *195*, 1266–1269.
21. Huang, P.; Heon, M.; Pech, D.; Brunet, M.; Taberna, P. L.; Gogotsi, Y.; Lofland, S.; Hettinger, J. D.; Simon, P. Micro-Supercapacitors from Carbide Derived Carbon (CDC) Films on Silicon Chips. *J. Power Sources* **2013**, *225*, 240–244.
22. Ahn, H.-J.; Kim, W. B.; Seong, T.-Y. $Co(OH)_2$-Combined Carbon-Nanotube Array Electrodes for High-Performance Micro-Electrochemical Capacitors. *Electrochem. Commun.* **2008**, *10*, 1284–1287.
23. Kim, D.; Shin, G.; Kang, Y. J.; Kim, W.; Ha, J. S. Fabrication of a Stretchable Solid-State Micro-supercapacitor Array. *ACS Nano* **2013**, *7*, 7975–7982.
24. Cai, Z. B.; Li, L.; Ren, J.; Qiu, L. B.; Lin, H. J.; Peng, H. S. Flexible, Weavable and Efficient Microsupercapacitor Wires Based on Polyaniline Composite Fibers Incorporated with Aligned Carbon Nanotubes. *J. Mater. Chem. A* **2013**, *1*, 258–261.
25. Shen, C. W.; Wang, X. H.; Zhang, W. F.; Kang, F. Y. A High-Performance Three-Dimensional Micro supercapacitor Based on Self-Supporting Composite Materials. *J. Power Sources* **2011**, *196*, 10465–10471.
26. Sun, W.; Zheng, R. L.; Chen, X. Y. Symmetric Redox Supercapacitor Based on Micro-fabrication with Three-Dimensional Polypyrrole Electrodes. *J. Power Sources* **2010**, *195*, 7120–7125.
27. Beidaghi, M.; Wang, C. L. Micro-supercapacitors Based on Three Dimensional Interdigital Polypyrrole/C-MEMS Electrodes. *Electrochim. Acta* **2011**, *56*, 9508–9514.
28. Chmiola, J.; Largeot, C.; Taberna, P.-L.; Simon, P.; Gogotsi, Y. Monolithic Carbide-Derived Carbon Films for Micro-supercapacitors. *Science* **2010**, *238*, 480–483.
29. Kim, M. S.; Hsia, B.; Carraro, C.; Maboudian, R. Flexible Micro-supercapacitors with High Energy Density from Simple Transfer of Photoresist-Derived Porous Carbon Electrodes. *Carbon* **2014**, *74*, 163–169.
30. Alper, J. P.; Kim, M. S.; Vincent, M.; Hsia, B.; Radmilovic, V.; Carraro, C.; Maboudian, R. Silicon Carbide Nanowires as Highly Robust Electrodes for Micro-Supercapacitor Applications. *J. Power Sources* **2013**, *230*, 298–302.
31. Shen, C. W.; Wang, X. H.; Li, S. W.; Wang, J. G.; Zhang, W. F.; Kang, F. Y. A High-Energy-Density Micro-supercapacitor of Asymmetric MnO_2−Carbon Configuration by Using Micro-fabrication Technologies. *J. Power Sources* **2013**, *234*, 302–309.
32. Wang, X. F.; Yin, Y. J.; Li, X. Y.; You, Z. Fabrication of a Symmetric Micro supercapacitor Based on Tubular Ruthenium Oxide on Silicon 3D Microstructures. *J. Power Sources* **2014**, *252*, 64–72.
33. Miller, J. R.; Outlaw, R. A.; Holloway, B. C. Graphene Double-Layer Capacitor with ac Line-Filtering Performance. *Science* **2010**, *329*, 1637–1639.
34. Niu, Z. Q.; Zhang, L.; Liu, L. L.; Zhu, B. W.; Dong, H. B.; Chen, X. D. All-Solid-State Flexible Ultrathin Micro-supercapacitors Based on Graphene. *Adv. Mater.* **2013**, *25*, 4035–4042.
35. Liu, W. W.; Feng, Y. Q.; Yan, X. B.; Chen, J. T.; Xue, Q. J. Superior Micro-supercapacitors Based on Graphene Quantum Dots. *Adv. Funct. Mater.* **2013**, *23*, 4111–4122.
36. Beidaghi, M.; Wang, C. L. Micro-supercapacitors Based on Interdigital Electrodes of Reduced Graphene Oxide and Carbon Nanotube Composites with Ultrahigh Power Handling Performance. *Adv. Funct. Mater.* **2012**, *22*, 4501–4510.
37. Lin, J.; Zhang, C. G.; Yan, Z.; Zhu, Y.; Peng, Z. W.; Hauge, R. H.; Natelson, D.; Tour, J. M. 3-Dimensional Graphene Carbon Nanotube Carpet-Based Micro-supercapacitors with High Electrochemical Performance. *Nano Lett.* **2013**, *13*, 72–78.
38. Wen, F. S.; Hao, C. X.; Xiang, J. Y.; Wang, L. M.; Hou, H.; Su, Z. B.; Hu, W. T.; Liu, Z. Y. Enhanced Laser Scribed Flexible Graphene-Based Micro-supercapacitor Performance with Reduction of Carbon Nanotubes Diameter. *Carbon* **2014**, *75*, 236–243.
39. Xue, M. Q.; Li, F. W.; Zhu, J.; Song, H.; Zhang, M. N.; Cao, T. B. Structure-Based Enhanced Capacitance: *In Situ* Growth of Highly Ordered Polyaniline Nanorods on Reduced Graphene Oxide Patterns. *Adv. Funct. Mater.* **2012**, *22*, 1284–1290.
40. Peng, L. L.; Peng, X.; Liu, B. R.; Wu, C. Z.; Xie, Y.; Yu, G. H. Ultrathin Two-Dimensional MnO_2/Graphene Hybrid Nanostructures for High-Performance, Flexible Planar Supercapacitors. *Nano Lett.* **2013**, *13*, 2151–2157.
41. Chen, J.; Bi, H.; Sun, S. R.; Tang, Y. F.; Zhao, W.; Lin, T. Q.; Wan, D. Y.; Huang, F. Q.; Zhou, X. D.; Xie, X. M.; *et al*. Highly Conductive and Flexible Paper of 1D Silver-Nanowire-Doped Graphene. *ACS Appl. Mater. Interfaces* **2013**, *5*, 1408–1413.
42. Williams, G.; Seger, B.; Kamat, P. V. TiO_2−Graphene Nanocomposites. UV-Assisted Photocatalytic Reduction of Graphene Oxide. *ACS Nano* **2008**, *2*, 1487–1491.
43. Zhu, J. H.; Chen, M. J.; Qu, H. L.; Luo, Z. P.; Wu, S. J.; Colorado, H. A.; Wei, S. Y.; Guo, Z. H. Magnetic Field Induced Capacitance Enhancement in Graphene and Magnetic Graphene Nanocomposites. *Energy Environ. Sci.* **2013**, *6*, 194–204.
44. Li, W. Y.; Xu, K. B.; An, L.; Jiang, F. R.; Zhou, X. Y.; Yang, J. M.; Chen, Z. G.; Zou, R. J.; Hu, J. Q. Effect of Temperature on the Performance of Ultrafine MnO_2 Nanobelt Supercapacitors. *J. Mater. Chem. A* **2014**, *2*, 1443–1448.
45. Zhu, S. W.; Gao, Y.; Hu, B.; Li, J.; Su, J.; Fan, Z. Y.; Zhou, J. Transferable Self-Welding Silver Nanowire Network as High Performance Transparent Flexible Electrode. *Nanotechnology* **2013**, *24*, 335202–335208.
46. Azhagan, M. V. K.; Vaishampayana, M. V.; Shelke, M. V. Synthesis and Electrochemistry of Pseudocapacitive Multilayer Fullerenes and MnO_2 Nanocomposites. *J. Mater. Chem. A* **2014**, *2*, 2152–2159.
47. Shi, J.-L.; Du, W.-C.; Yin, Y.-X.; Guo, Y.-G.; Wan, L.-J. Hydrothermal Reduction of Three-Dimensional Graphene Oxide for Binder-Free Flexible Supercapacitors. *J. Mater. Chem. A* **2014**, *2*, 10830–10834.
48. Yuan, L. Y.; Lu, X.-H.; Xiao, X.; Zhai, T.; Dai, J. J.; Zhang, F. C.; Hu, B.; Wang, X.; Gong, L.; Chen, J.; *et al*. Flexible Solid-State Supercapacitors Based on Carbon Nanoparticles/MnO_2 Nanorods Hybrid Structure. *ACS Nano* **2012**, *6*, 656–661.
49. Yu, Z. N.; Li, C.; Abbitt, D.; Thomas, J. Flexible, Sandwich-like Ag-Nanowire/PEDOT: PSS-Nanopillar/MnO_2 High Performance Supercapacitors. *J. Mater. Chem. A* **2014**, *2*, 10923–10929.
50. Ding, Y.; Wang, Y.; Su, L.; Zhang, H.; Lei, Y. Preparation and Characterization of NiO-Ag Nanofibers, NiO Nanofibers, and Porous Ag: Towards the Development of a Highly Sensitive and Selective Non-enzymatic Glucose Sensor. *J. Mater. Chem.* **2010**, *20*, 9918–9926.
51. Lang, X. Y.; Hirata, A.; Fujita, T.; Chen, M. W. Nanoporous Metal/Oxide Hybrid Electrodes for Electrochemical Supercapacitors. *Nat. Nanotechnol.* **2011**, *6*, 232–236.
52. Xiao, X.; Li, T. Q.; Yang, P. H.; Gao, Y.; Jin, H. Y.; Ni, W. J.; Zhan, W. H.; Zhang, X. H.; Cao, Y. Z.; Zhong, J. W.; *et al*. Fiber-Based All-Solid-State Flexible Supercapacitors for Self-Powered Systems. *ACS Nano* **2012**, *6*, 9200–9206.
53. Dinh, T. M.; Armstrong, K.; Guay, D.; Pech, D. High-Resolution on-Chip Supercapacitors with Ultra-high Scan Rate Ability. *J. Mater. Chem. A* **2014**, *2*, 7170–7174.
54. Fu, Y. P.; Cai, X.; Wu, H. W.; Lv, Z. B.; Hou, S. C.; Peng, M.; Yu, X.; Zou, D. C. Fiber Supercapacitors Utilizing Pen Ink for Flexible/Wearable Energy Storage. *Adv. Mater.* **2012**, *24*, 5713–5718.
55. Si, W. P.; Yan, C. L.; Chen, Y.; Oswald, S.; Han, L. Y.; Schmidtabde, O. G. On Chip, All Solid-State and Flexible

Micro-supercapacitors with High Performance Based on MnO_x/Au Multilayers. *Energy Environ. Sci.* **2013**, *6*, 3218–3223.
56. Lee, J. A.; Shin, M. K.; Kim, S. H.; Cho, H. U.; Spinks, G. M.; Wallace, G. G.; Lima, M. D.; Lepro, X.; Kozlov, M. E.; Baughman, R. H.; *et al*. Ultrafast Charge and Discharge Biscrolled Yarn Supercapacitors for Textiles and Microdevices. *Nat. Commun.* **2013**, *4*, 1970–1977.
57. Gogotsi, Y.; Simon, P. True Performance Metrics in Electrochemical Energy Storage. *Science* **2011**, *334*, 917–918.
58. Wei, L.; Sevilla, M.; Fuertes, A. B.; Mokaya, R.; Yushin, G. Hydrothermal Carbonization of Abundant Renewable Natural Organic Chemicals for High-Performance Supercapacitor Electrodes. *Adv. Energy Mater.* **2011**, *1*, 356–361.
59. Chen, L. Y.; Hou, Y.; Kang, J. L.; Hirata, A.; Fujita, T.; Chen, M. W. Toward the Theoretical Capacitance of RuO_2 Reinforced by Highly Conductive Nanoporous Gold. *Adv. Energy Mater.* **2013**, *3*, 851–856.
60. Xu, Y. F.; Hennig, I.; Freyberg, D.; Strudwick, A. J.; Schwab, M. G.; Weitz, T.; Cha, K. C.-P. Inkjet-Printed Energy Storage Device Using Graphene/Polyaniline Inks. *J. Power Sources* **2014**, *248*, 483–488.
61. Li, H. B.; Yu, M. H.; Wang, F. X.; Liu, P.; Liang, Y.; Xiao, J.; Wang, C. X.; Tong, Y. X.; Yang, G. W. Amorphous Nickel Hydroxide Nanospheres with Ultrahigh Capacitance and Energy Density as Electrochemical Pseudocapacitor Materials. *Nat. Commun.* **2013**, *4*, 1894–1901.
62. Lee, S.; Ha, J.; Jo, S.; Choi, J.; Song, T.; Park, W. I.; Rogers, J. A.; Paik, U. LEGO-like Assembly of Peelable, Deformable Components for Integrated Devices. *NPG Asia Materials* **2013**, *5*, 66–71.
63. Wishart, J. F. Energy Applications of Ionic Liquids. *Energy Environ. Sci.* **2009**, *2*, 956–961.
64. Zhao, J. P.; Pei, S. F.; Ren, W. C.; Gao, L. B.; Cheng, H. M. Efficient Preparation of Large-Area Graphene Oxide Sheets for Transparent Conductive Films. *ACS Nano* **2010**, *4*, 5245–5252.
65. Zhang, X.; Yan, X. B.; Chen, J. T.; Zhao, J. P. Large-Size Graphene Microsheets as a Protective Layer for Transparent Conductive Silver Nanowire Film Heaters. *Carbon* **2014**, *69*, 437–443.
66. Chen, S.; Zhu, J. W.; Wu, X. D.; Han, Q. F.; Wang, X. Graphene Oxide–MnO_2 Nanocomposites for Supercapacitors. *ACS Nano* **2010**, *4*, 2822–2830.
67. Wang, S.; Hsia, B.; Carraro, C.; Maboudian, R. High-Performance All Solid-State Micro-supercapacitor Based on Patterned Photoresist Derived Porous Carbon Electrodes and an Ionogel Electrolyte. *J. Mater. Chem. A* **2014**, *2*, 7997–8002.